PAPER

Characterization of charge transport properties of a 3D electrode for dye-sensitized solar cells†

Chang-Yeol Cho, Hye-Na Kim and Jun Hyuk Moon*

Electron transport and recombination in three-dimensionally-ordered (3D-ordered) structure electrodes were investigated using intensity-modulated photocurrent and photovoltage spectroscopy. The surface-modified TiO_2 inverse opal structure was applied as a 3D electrode. The morphology, crystalline structure and surface states of the 3D-ordered structure were characterized by SEM, TEM and XPS and compared to those of the conventional nanoparticulate TiO_2 structure. The performance of the 3D electrode was also evaluated by comparing the transport time and recombination lifetime to those of the conventional electrodes. Remarkably, the recombination lifetime in inverse opal was found to be greater than in nanocrystalline TiO_2 by 4.3–6.2 times, thus improving the electron collection efficiency by 10%. Comparing the photovoltaic performance, although the dye adsorption of the 3D-ordered porous electrode is lower, the electrode achieves a photocurrent density comparable to that of a nano-particulate TiO_2 electrode due to the higher light scattering as well as the higher collection efficiency.

1. Introduction

Dye-sensitized solar cells (DSSCs) are a promising photovoltaic technology due to their relatively low cost and high conversion efficiency.[1,2] DSSCs are composed of a photo-electrode, with a TiO_2 semiconductor layer sensitized by dye molecules, and a platinized counter electrode. In a conventional DSSC, spherical TiO_2 nanoparticles of around 20 nm diameter are used in the semiconductor layer. The electrode then possesses similar sized voids around the nanoparticles. An electrolyte solution fills these voids, as well as the gap between the two electrodes. Efficiencies of up to 11–12% have been achieved with this type of electrode.[3] However, the randomly packed structure leads to long electron diffusion pathways, which is inferred to be a source of inefficiency of these DSSCs. The diffusion rate in nanocrystalline TiO_2 was measured to be orders of magnitude lower than in the bulk material.[4–6] Moreover, the close contact between TiO_2 and oxidizing species in the electrolyte is expected to induce high rates of charge recombination with electrolyte triiodide ions when electron diffusion away from the interface is slow.[7] Recent results employing one-dimensional (1D) electrodes consisting of nanorods, nanowires, nanofibers, and ordered arrays

of nanotubes showed directional transport of electrons and lower recombination.[8–14] More recently, 3D structures such as inverse opal-based structures and interference lithography patterns have also been introduced as alternative electrode materials.[15–18]

An understanding of how transport and recombination properties are related to the morphology of electrode structures and a comparison of these properties in newly designed electrodes to those of conventional TiO_2 electrodes are important for the further design of new electrode materials.[8,19,20] TiO_2 rutile nanowire electrodes showed much higher diffusion coefficients than conventional electrodes at the same electron density.[8] In the case of TiO_2 nanotube electrodes, a recombination lifetime 10 times greater than conventional electrodes was measured.[19] Electrodes composed of hollow TiO_2 fibers were found to have a transport time and recombination lifetime 3 times greater and 2–3 times greater than conventional electrodes, respectively.[11] In spite of these promising transport properties, these structures yielded a lower incident photon-to-current efficiency (IPCE) than conventional DSSCs. But, the potential gains in cell performance mean that the optimization of electrode transport properties is still a worthwhile endeavor. For example, enhanced electron transport has enabled the application of an alternative redox electrolyte, which shows relatively fast electron-interception but has a more positive redox potential, leading to improvement in the open circuit voltage of the cell and therefore the efficiency.[9,21]

In this report, we characterize the morphology and electron transport dynamics of 3D ordered structure electrodes for DSSCs.

Department of Chemical and Biomolecular Engineering, Sogang University,
1 Sinsu-dong, Mapo-gu, Seoul, Republic of Korea. E-mail: junhyuk@sogang.ac.kr;
Fax: +82 2 703 8971; Tel: +82 2 705 8921
† Electronic supplementary information (ESI) available. See DOI: 10.1039/c3cp50214g

This journal is © the Owner Societies 2013

Phys. Chem. Chem. Phys., 2013, **15**, 10835–10840 | **10835**

The electron transport dynamics were compared with those of a commercial nanoparticle TiO$_2$ (NP-TiO$_2$) electrode. Many previous reports have analyzed the transport and recombination properties of electrodes based on 1D morphologies. On the other hand, there have been few reports of the study of 3D structured electrodes. In this work, 3D ordered structures were fabricated by the colloidal templating approach, as described elsewhere.[22] Transport and recombination properties were evaluated by intensity-modulated photocurrent spectroscopy (IMPS) and intensity-modulated photovoltage spectroscopy (IMVS) and compared with conventional TiO$_2$ electrodes. The photovoltaic properties of 3D ordered porous electrodes and conventional electrodes were also compared.

2. Experimental

Fabrication of TiO$_2$ inverse opal-based electrodes

Polystyrene (PS) spheres were obtained by dispersion polymerization of styrene monomers, as reported elsewhere; PS particles of 700 nm diameter redispersed in aqueous solution were obtained. The aqueous colloid of TiO$_2$ nanoparticles (average size 15 nm, Nanoamor Inc.) was infiltrated into the PS colloidal crystal template. The sample was heat-treated at 500 °C for 2 h in air, leaving behind inverse opals. To fabricate the pIO-TiO$_2$ structures, inverse opal electrodes were soaked in 0.3 M TiCl$_4$ aqueous solution at 70 °C for 1 h. To make the comparison nanocrystalline TiO$_2$ electrode, commercial TiO$_2$ colloidal paste (Dyesol, 18NR-T) was doctor-bladed onto an FTO substrate. The post-treatment in 0.3 M TiCl$_4$ aqueous solution at 70 °C for 30 min was achieved. The sample was heat-treated at 500 °C for 2 h in air.

DSSC assembly

Sensitization was achieved by soaking electrodes in a 0.5 mM N719 (Solaronix) dye solution in anhydrous ethanol (99.9%, Aldrich) for 1 day at room temperature. Subsequently, the dye-adsorbed electrodes were rinsed thoroughly with anhydrous ethanol and dried in air. They were assembled with a platinum counter electrode using Surlyn film (60 μm, Dupont) as a spacer. Finally, the liquid electrolyte was introduced into the gap between electrodes; the electrolyte was formulated by mixing 0.7 M 1-butyl-3-methyl-imidazolium iodide (Sigma-Aldrich), 0.03 M I$_2$ (Yakuri), 0.05 M LiI (Sigma-Aldrich) and 0.5 M 4-*t*-butylpyridine (Aldrich) in a solution of acetonitrile (Aldrich).

Characterization

The *J*–*V* characteristics of the DSSCs were measured using a source meter (Keithley Instruments) under simulated solar light, which was provided by a solar simulator (1000 W Xe lamp with AM 1.5G filter, PEC-L01, Peccell Technologies). The light intensity was adjusted to 100 mW cm^{-2} using a Si reference cell (BS-520, Bunko-Keiki). The charge transport properties were measured by intensity modulated photocurrent spectroscopy (IMPS) and intensity modulated voltage spectroscopy (IMVS). The intensity modulated measurements were carried out using a frequency response analyzer (XPOT, Zahner),

which was used to drive a green light emitting diode (520 nm). The LED provided both the DC and AC component of the illumination. The modulation amplitude of the AC component superimposed on the DC component was 10%. SEM images were obtained using a field-emission scanning electron microscope (FE-SEM, Hitachi S-4700). TEM images were obtained using a 300 kV high-resolution transmission electron microscope (JEM-3010, JEOL). The chemical components of the TiO$_2$ surface were analyzed by X-ray photoelectron spectroscopy (XPS, ESCALAB 250 XPS System, Thermo Fisher Scientific) using a monochromated Al Kα X-ray source at 1486.6 eV. The amount of dye absorption was evaluated by measuring the absorption of dye molecules detached from sensitized TiO$_2$ surfaces *via* UV-Vis spectrophotometry (UV-2550, Shimadzu). The dye on a known TiO$_2$ electrode area was detached *via* immersion in a 0.1 M NaOH solution. The incident photon-to-current conversion efficiency (IPCE) was measured using a 300 W Xe light source, (Oriel) with a monochromator and in dc mode. The incident light intensity was measured using a photodiode detector (silicon calibrated detector, Newport).

3. Results and discussion

3D ordered structures were obtained using colloidal crystal templates. We employed post-treated inverse opal (pIO) structures. The pIO structure was fabricated by the additional precursor treatment of IO structures.[22] Fig. 1a and b show a SEM micrograph of the skeleton and the post-treated IO TiO$_2$ (pIO) structure, respectively. pIO possessed pores that were ordered and fully connected in 3D, as shown in Fig. 1a; specifically the structure possessed 550–600 nm macropores, with each pore interconnected by smaller pores of 100–150 nm diameter. The pIO structure includes a bilayer comprising the TiO$_2$ IO skeleton and the post-treated layer. The IO skeleton has a thickness of around 60 nm and consists of closely packed spherical TiO$_2$ nanoparticles (around 10 nm in diameter), as shown in Fig. 1c. The post-treated layer is composed of loosely grown rod-like rutile particles (see Fig. S1 and S2, ESI†) with a
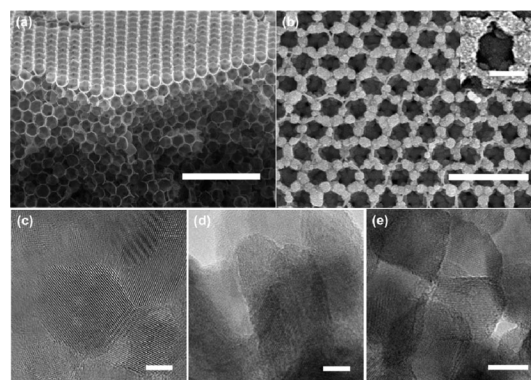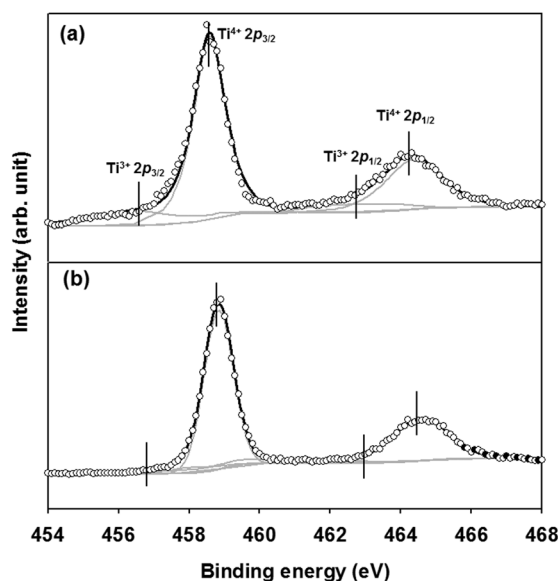

Fig. 1 SEM images of the (a) IO-TiO$_2$ structure, (b) surface of pIO-TiO$_2$; high resolution TEM images of (c) the IO TiO$_2$ structure, (d) the pIO-TiO$_2$ structure, (e) the NP-TiO$_2$. The inset in (b) shows SEM images of pIO macropores for the sample shown in (b). Scale bar: (a) 5 μm; (b) 2.5 μm (c–e) 5 nm; inset in (b) 500 nm.

Table 1 The photovoltaic parameters of DSSCs containing pIO-TiO$_2$ and NP-TiO$_2$ electrodes under simulated AM 1.5G conditions, extracted from the J–V curve

	Average dye adsorption (μmol cm^{-3})	V_{OC} (V)	J_{sc} (mA cm^{-2})	FF	Efficiency (%)
pIO-TiO$_2$	0.0249	0.72	12.69	0.61	5.60
NP-TiO$_2$	0.0625	0.76	12.38	0.65	6.12

thickness of around 90–140 nm; the single rutile TiO$_2$ particles are around 10 × 30 nm in size. For comparison, we show in Fig. 1d a TEM micrograph of TiO$_2$ nanoparticles in a conventional electrode film (Dyesol 18NR-T). The film is composed of TiO$_2$ nanoparticles around 10 nm in diameter, and the voids around the TiO$_2$ particles are 10–20 nm, as shown in Fig. 1e.

Film surface areas were estimated by measuring the adsorbed dye concentration, as listed in Table 1; we found that the adsorbed density on the NP film was 2.5 ± 0.2 times higher than that on the pIO film, based on the average of 10 samples. The lower specific area of pIO was attributed to the presence of macropores. The chemical states of the pIO and NP-TiO$_2$ films were investigated by X-ray photoelectron spectroscopy (XPS). The oxidation state and concentration of oxygen vacancies in a TiO$_2$ surface affect the electron transport/recombination as well as the efficiency of dye adsorption.[23,24] Fig. 2a and b show the Ti 2p photoelectron spectra of NP and pIO films, respectively. Four peaks (Ti^{4+} 2p$_{1/2}$, Ti^{3+} 2p$_{1/2}$, Ti^{4+} 2p$_{3/2}$, and Ti^{3+} 2p$_{3/2}$) were used to deconvolve the spectra. The main peaks at 458.6 eV and 464.3 eV were attributed to Ti^{4+} or TiO$_2$, while the peaks at 457.0 eV and 462.8 eV correspond to Ti^{3+} surface states, i.e., oxygen vacancies.[25] The TiO$_2$ surface of the NP film showed peak intensities corresponding to a relatively high concentration of defect states compared to the pIO film. We also compared the
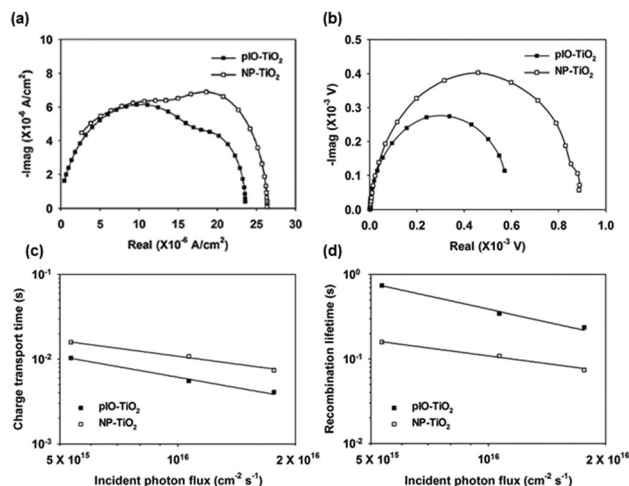
Fig. 3 Typical (a) IMPS and (b) IMVS responses of p-IO TiO$_2$ and np-TiO$_2$ based DSSCs, incident photon flux dependence of (c) transport time and (d) recombination lifetime for pIO-TiO$_2$ and NP-TiO$_2$ based DSSCs.

XPS spectra of IO and pIO films as shown in Fig. S3 (ESI†). The intensity of peaks related to the Ti^{3+} surface states in IO-TiO$_2$ was similar to those of pIO-TiO$_2$. This confirms that the lower defect states in pIO films were not attributed to longer TiCl$_4$ treatment, but rather to intrinsic properties of the TiO$_2$ layer coated on the IO structure.[26] TiO$_2$ surfaces with fewer defects have improved electron transport, because oxygen vacancies hinder electron movement by trapping and de-trapping.[26]

IMPS and IMVS measurements were carried out for NP and 3D pIO electrodes, and their transport and recombination characteristics were compared. Fig. 3a shows typical IMPS responses for the two electrodes at a photon flux of 1.76 × 10^{16} cm^{-2} s^{-1}. The IMPS graphs show two semicircles, implying two distinct modes of electron transport. The semicircles at high and low frequencies have previously been attributed to trap-delayed electron transport far from and near to the collecting substrate, respectively.[27] Comparing the ratio of the high-frequency semicircle radius to the low-frequency semicircle radius, in Fig. 3a the pIO electrodes show a larger ratio than that of the NP electrodes; this suggests that the electron-filled trap layers near the collecting substrate in pIO electrodes are thicker than those in NP. This result implies that pIO-TiO$_2$ structures possess a lower density of traps, or transport electrons along shorter paths due to the ordered structure.

The transport times of pIO and NP electrodes were measured as a function of the incident photon flux; results are shown in Fig. 3c. The charge transport time (τ_c) was estimated from the frequency minimum of the IMPS imaginary component, $\tau_c = 1/2\pi f_c$.[5,28] The power law dependence of τ_c on the photon flux was measured for both electrodes; this nonlinear sensitivity to photon flux reflects the fact that electron transport is governed by a random walk between traps and a power-law distribution of trapping time.[4–6,29,30] In Fig. 3c, it is noted that the 3D pIO electrode was found to have a shorter τ_c than that of the NP electrode: τ_c of pIO was 1.9–2.3 times shorter than that of NP over the measured range of photon flux.

Fig. 2 XPS Ti 2p spectrum of (a) the NP-TiO$_2$ and (b) the pIO-TiO$_2$ structure; experimental data (circle), four deconvolved spectra (gray solid line), summation of the four spectra (black solid line).

It has been reported that τ_c is related to the volumetric trap density N_t in the form of $\tau_c \propto N_t^{2/3}$ under the same incident light intensity, and other constants like electrode film thickness and electron mobility.[5] This equation can be modified to give $\tau_c \propto$ (specific area)$^{2/3}$ because the trap states have been reported to be predominantly located on the surface of the TiO$_2$ nanoparticles rather than in the bulk.[5,31,32] This relation was used to exclude the effect of the specific area on τ_c, by normalization of the specific area. Considering the specific area evaluated by the measurement of dye adsorption was around 2.5 times higher for NP electrodes than for pIO, the τ_c of the pIO structure was estimated to be 3–25% shorter than in the NP structure. Thus, the area-normalized τ_c revealed a slightly large pIO structure compared with NP.

We also analyzed the IMVS responses of pIO and NP electrodes. Fig. 3b shows the IMVS results at a photon flux of 1.76×10^{16} cm^{-2} s^{-1}. The electron lifetime (τ_r) was extracted from the characteristic frequency at the minimum of the IMVS imaginary component, that is, $\tau_r = 1/2\pi f_r$.[5,28] The recombination lifetimes of pIO and NP electrodes are shown in Fig. 3d as a function of the incident photon flux. The power law dependence of the lifetime on the incident photon flux also reveals the charge recombination during the trap-limited transport. Over the measured range of photon flux, τ_r of the pIO electrode was 3.2–4.6 times larger than that of the NP electrode. We also obtained the area-normalized τ_r similar to the previous analysis. It has been reported that the recombination lifetime shortened with decreasing particle size, which increases the specific area of the electrode; empirical fitting of recombination current density vs. roughness factor (or specific area of the electrode) provided the relationship $\tau_r \propto$ (specific area)$^{-0.33}$.[33] Based on this relation, the area-normalized value for τ_r of the pIO electrode was 4.3–6.2 times greater than that of the NP electrode. In contrast to the normalized τ_c, the value of the area normalized τ_r for the pIO electrode was much larger compared to the NP structure.

The measurement of area-normalized transport and recombination lifetimes revealed that only τ_r was much higher for the 3D pIO-TiO$_2$ electrode than for the NP-TiO$_2$ electrode, while τ_c of the pIO electrode was only up to 25% higher than that of the NP electrode. Since both electron transport and recombination lifetimes showed power-law dependence, both processes are governed by trap-limited transport. Then, one would thus expect that there be a similar degree of enhancement in both τ_r and τ_c (ref. 34) in pIO structures, compared to NP structures. However in this work, assuming the same specific area among the electrodes, τ_r in pIO was enhanced significantly more than τ_c. This may be due to the less defective surfaces of the pIO structure, as shown in the XPS results. The lower defect density effectively decreased electron trapping and reduced recombination. Another possible explanation may be that the more compact packing of TiO$_2$ nanoparticles in the IO skeleton results in less contact with the electrolyte, lowering charge recombination. Meanwhile, the less-than-expected enhancement in τ_c compared with τ_r may be attributed to the rutile structure of the TiO$_2$ particles in the pIO structure. Park et al. observed that
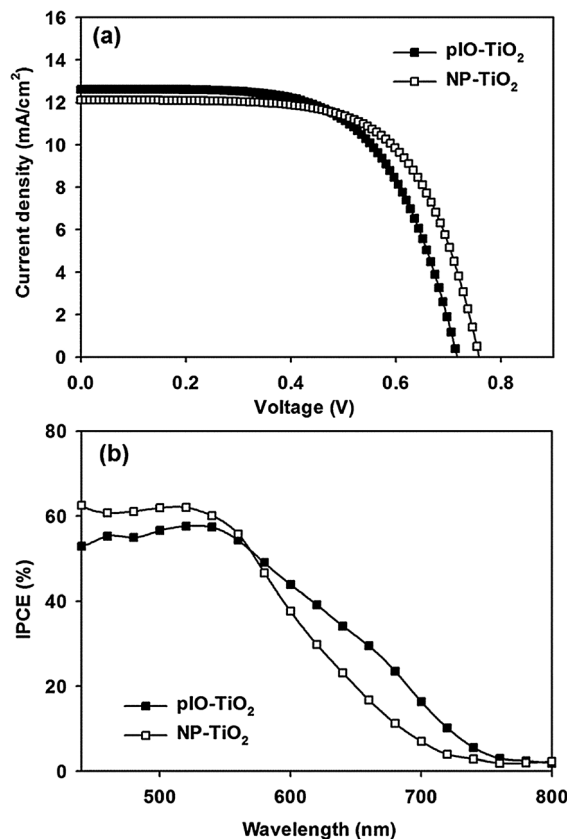

Fig. 4 (a) J–V curves and (b) IPCE spectra of the pIO-TiO$_2$ electrode and the NP-TiO$_2$ electrode for dye-sensitized solar cells.

charge transport was slower in rutile layers than in anatase layers.[35] The rod-shaped rutile particles possess less interconnectivity than spherical anatase particles, resulting in less efficient electron transport.

Fig. 4 and Table 1 show the photocurrent density and voltage (J–V) properties of DSSCs with NP and pIO-TiO$_2$ electrodes under AM 1.5G illumination. The thickness and area of both electrode films were kept at 8 μm and 5 mm × 5 mm, respectively. It is noteworthy that the photocurrent density (J_{sc}) of the pIO electrode was comparable (3% lower) to that of the NP electrode even though the dye adsorption density of the pIO electrode was 40% that of the NP electrode. J_{sc} is defined by multiplication of the light-harvesting efficiency, electron injection into the electrode, and collection by the FTO substrate.[1] First, the light-harvesting efficiency was mainly determined by the amount of dye adsorption and light scattering behavior.[21] Although pIO electrodes had lower dye adsorption than NP electrodes due to the presence of macropores, the macropores induced Mie scattering (see Fig. S4, ESI†), which elongates the optical path length of incident light and thereby enhances light absorption. As shown in Fig. 4b, the IPCE of DSSCs with the pIO electrodes was 2–5% higher than that of the NP electrodes in the wavelength range between 580 nm and 800 nm due to the scattering. This effect compensates for the loss in light harvesting efficiency due to the lower density of dye molecules.[36] Second, the collection efficiency

can be approximated using the transport and recombination lifetime; the charge collection efficiency η_{cc} can be determined from the equation, $\eta_{cc} = 1 - (\tau_c/\tau_r)$.[28]

At an incident photon flux of 1.76×10^{16} cm^{-2} s^{-1}, τ_c and τ_r values for the NP electrodes were 0.0074 s and 0.074 s, respectively and η_{cc} of the NP electrodes was 90%. Considering the area-normalized τ_c and τ_r values for the pIO electrodes, η_{cc} of the pIO electrode was around 98%, almost 10% larger. Third, electron injection into the pIO-TiO$_2$ might be lower than injection into NP-TiO$_2$. The conduction band of rutile TiO$_2$ is slightly higher than anatase TiO$_2$.[37,38] The band edge of rutile was measured to be shifted higher in energy by 0.2 eV compared to anatase. Finally, we can conclude that the comparable J_{sc} result for the two electrodes is attributed to higher light harvesting efficiency and electron collection efficiency by the pIO-TiO$_2$ electrodes.

4. Conclusion

In summary, we characterized the electron transport and recombination times of the 3D periodic TiO$_2$ structured electrode for DSSCs, and compared the results with those of NP-TiO$_2$ electrodes with the same thickness. The IO-based electrode was adopted as a 3D electrode. The values of τ_c and τ_r of DSSCs containing 3D pIO electrodes were measured using IMVS and IMPS measurements. First, pIO electrodes displayed power-law dependence for both τ_c and τ_r on the incident photon flux, which implies trap-limited electron transport similar to NP-TiO$_2$ electrodes. Second, the surface area-normalized τ_c and τ_r of the pIO electrode were estimated to be 3–25% and 4.3–6.5 times higher than in the NP electrode, respectively. Thus, the enhancement in electron transport and recombination properties was caused by the 3D connected structures within the pIO-TiO$_2$ electrodes. The relatively large enhancement in τ_r compared to τ_c in the pIO electrode may be attributed to the less defective surfaces of pIO-TiO$_2$, compact packing of the TiO$_2$ nanoparticles in the IO skeleton, and the presence of a rutile TiO$_2$ layer. Previous experiments comparing 1D TiO$_2$ nanotube arrays and conventional TiO$_2$ (similar to our NP-TiO$_2$) electrodes showed that the value of τ_c was similar but τ_r was remarkably enhanced by 10 times.[19] The electrodes comprising electrospun 1D TiO$_2$ nanorod electrodes also showed 8 times longer τ_r compared with conventional TiO$_2$ electrodes.[39] Thus, it can be expected that 3D electrodes show a comparable charge transport enhancement to 1D electrodes. The photovoltaic parameters of DSSCs containing pIO electrodes were also compared with the performance using NP electrodes. The efficiency of the pIO electrode was 10% lower but J_{sc} was comparable to the NP-TiO$_2$ electrode; this was due to the higher η_{cc} and scattering in the pIO structure.

Although the 3D ordered structure electrode showed lower conversion efficiency than the conventional electrode, more open and connected pore structures induce facile infiltration of viscous quasi-solid or solid electrolytes for solid-state dye solar cells.[40] Thus, the decrease in efficiency that usually occurs due to lower infiltration by these electrolytes into the NP-TiO$_2$ electrodes can be overcome. Moreover, these pore structures may be well suited to the recent approach of introducing quantum-dot nanoparticles instead of sensitizing molecules.[41,42]

Acknowledgements

Notes and references

1 B. Oregan and M. Gratzel, *Nature*, 1991, **353**, 737–740.
2 M. K. Nazeeruddin, A. Kay, I. Rodicio, R. Humphrybaker, E. Muller, P. Liska, N. Vlachopoulos and M. Gratzel, *J. Am. Chem. Soc.*, 1993, **115**, 6382–6390.
3 A. Yella, H. W. Lee, H. N. Tsao, C. Y. Yi, A. K. Chandiran, M. K. Nazeeruddin, E. W. G. Diau, C. Y. Yeh, S. M. Zakeeruddin and M. Gratzel, *Science*, 2011, **334**, 629–634.
4 A. Solbrand, H. Lindstrom, H. Rensmo, A. Hagfeldt, S. E. Lindquist and S. Sodergren, *J. Phys. Chem. B*, 1997, **101**, 2514–2518.
5 J. van de Lagemaat and A. J. Frank, *J. Phys. Chem. B*, 2001, **105**, 11194–11205.
6 N. W. Duffy, L. M. Peter and K. G. U. Wijayantha, *Electrochem. Commun.*, 2000, **2**, 262–266.
7 J. Nelson, S. A. Haque, D. R. Klug and J. R. Durrant, *Phys. Rev. B: Condens. Matter Mater. Phys.*, 2001, **63**, 205321.
8 X. Feng, K. Zhu, A. J. Frank, C. A. Grimes and T. E. Mallouk, *Angew. Chem., Int. Ed.*, 2012, **51**, 2727.
9 A. B. F. Martinson, M. S. Goes, F. Fabregat-Santiago, J. Bisquert, M. J. Pellin and J. T. Hupp, *J. Phys. Chem. A*, 2009, **113**, 4015–4021.
10 K. Zhu, N. R. Neale, A. F. Halverson, J. Y. Kim and A. J. Frank, *J. Phys. Chem. C*, 2010, **114**, 13433–13441.
11 E. Ghadiri, N. Taghavinia, S. M. Zakeeruddin, M. Gratzel and J. E. Moser, *Nano Lett.*, 2010, **10**, 1632–1638.
12 X. Q. Gu, Y. L. Zhao and Y. H. Qiang, *J. Mater. Sci.: Mater. Electron.*, 2012, **23**, 1373–1377.
13 D. Hwang, S. M. Jo, D. Y. Kim, V. Armel, D. R. MacFarlane and S. Y. Jang, *ACS Appl. Mater. Interfaces*, 2011, **3**, 1521–1527.
14 L. J. Yang and W. W. F. Leung, *Adv. Mater.*, 2011, **23**, 4559–4562.
15 W. M. Jin, J. H. Shin, C. Y. Cho, J. H. Kang, J. H. Park and J. H. Moon, *ACS Appl. Mater. Interfaces*, 2010, **2**, 2970–2973.
16 C. Y. Cho and J. H. Moon, *Adv. Mater.*, 2011, **23**, 2971–2975.
17 Y. G. Seo, K. Woo, J. Kim, H. Lee and W. Lee, *Adv. Funct. Mater.*, 2011, **21**, 3094–3103.
18 C. Y. Cho and J. H. Moon, *Langmuir*, 2012, **28**, 9372–9377.
19 K. Zhu, N. R. Neale, A. Miedaner and A. J. Frank, *Nano Lett.*, 2007, **7**, 69–74.
20 M. Law, L. E. Greene, J. C. Johnson, R. Saykally and P. D. Yang, *Nat. Mater.*, 2005, **4**, 455–459.
21 A. Listorti, B. O'Regan and J. R. Durrant, *Chem. Mater.*, 2011, **23**, 3381–3399.

This journal is © the Owner Societies 2013

Phys. Chem. Chem. Phys., 2013, **15**, 10835–10840 | **10839**

22 J. H. Shin and J. H. Moon, *Langmuir*, 2011, **27**, 6311–6315.

23 J. Weidmann, T. Dittrich, E. Konstantinova, I. Lauermann, I. Uhlendorf and F. Koch, *Sol. Energy Mater. Sol. Cells*, 1999, **56**, 153–165.

24 H. L. Wang, J. J. He, G. Boschloo, H. Lindstrom, A. Hagfeldt and S. E. Lindquist, *J. Phys. Chem. B*, 2001, **105**, 2529–2533.

25 W. Y. Wu, T. W. Shih, P. Chen, J. M. Ting and J. M. Chen, *J. Electrochem. Soc.*, 2011, **158**, K101–K106.

26 P. M. Sommeling, B. C. O'Regan, R. R. Haswell, H. J. P. Smit, N. J. Bakker, J. J. T. Smits, J. M. Kroon and J. A. M. van Roosmalen, *J. Phys. Chem. B*, 2006, **110**, 19191–19197.

27 P. T. Hsiao, Y. L. Tung and H. S. Teng, *J. Phys. Chem. C*, 2010, **114**, 6762–6769.

28 G. Schlichthorl, N. G. Park and A. J. Frank, *J. Phys. Chem. B*, 1999, **103**, 782–791.

29 J. Nelson and R. E. Chandler, *Coord. Chem. Rev.*, 2004, **248**, 1181–1194.

30 F. Cao, G. Oskam, G. J. Meyer and P. C. Searson, *J. Phys. Chem.*, 1996, **100**, 17021–17027.

31 N. Kopidakis, N. R. Neale, K. Zhu, J. van de Lagemaat and A. J. Frank, *Appl. Phys. Lett.*, 2005, **87**, 202106.

32 J. A. Anta and V. Morales-Florez, *J. Phys. Chem. C*, 2008, **112**, 10287–10293.

33 K. Zhu, N. Kopidakis, N. R. Neale, J. van de Lagemaat and A. J. Frank, *J. Phys. Chem. B*, 2006, **110**, 25174–25180.

34 N. Kopidakis, K. D. Benkstein, J. van de Lagemaat and A. J. Frank, *J. Phys. Chem. B*, 2003, **107**, 11307–11315.

35 N. G. Park, J. van de Lagemaat and A. J. Frank, *J. Phys. Chem. B*, 2000, **104**, 8989–8994.

36 S. Hore, P. Nitz, C. Vetter, C. Prahl, M. Niggemann and R. Kern, *Chem. Commun.*, 2005, 2011–2013.

37 P. Deak, B. Aradi and T. Frauenheim, *J. Phys. Chem. C*, 2011, **115**, 3443–3446.

38 L. Kavan, M. Gratzel, S. E. Gilbert, C. Klemenz and H. J. Scheel, *J. Am. Chem. Soc.*, 1996, **118**, 6716–6723.

39 B. H. Lee, M. Y. Song, S. Y. Jang, S. M. Jo, S. Y. Kwak and D. Y. Kim, *J. Phys. Chem. C*, 2009, **113**, 21453–21457.

40 M.-S. Kang, J. H. Kim, Y. J. Kim, J. Won, N. G. Park and Y. S. Kang, *Chem. Commun.*, 2005, 889.

41 S. K. Karuturi, J. S. Luo, C. W. Cheng, L. J. Liu, L. T. Su, A. I. Y. Tok and H. J. Fan, *Adv. Mater.*, 2012, **24**, 4157–4162.

42 T. Toyoda and Q. Shen, *J. Phys. Chem. Lett.*, 2012, **3**, 1885–1893.